

Neural-Network Chemical Emulator for First-Star Formation: Robust Iterative Predictions over a Wide Density Range

SOJUN ONO ^{1,2} AND KAZUYUKI SUGIMURA ²

¹*Department of Astronomy, Kyoto University, Kitashirakawa-Oiwake-cho, Sakyo-ku, Kyoto 606-8502, Japan*

²*Faculty of Science, Hokkaido University, Sapporo, Hokkaido 060-0810, Japan*

ABSTRACT

We present a neural-network emulator for the thermal and chemical evolution in Population III star formation. The emulator accurately reproduces the thermochemical evolution over a wide density range spanning 21 orders of magnitude (10^{-3} – 10^{18} cm⁻³), tracking six primordial species: H, H₂, e⁻, H⁺, H⁻, and H₂⁺. To handle the broad dynamic range, we partition the density range into five subregions and train separate deep operator networks (DeepONets) in each region. When applied to randomly sampled thermochemical states, the emulator achieves relative errors below 10 % in over 90 % of cases for both temperature and chemical abundances (except for the rare species H₂⁺). The emulator is roughly ten times faster on a CPU and more than 1000 times faster for batched predictions on a GPU, compared with conventional numerical integration. Furthermore, to ensure robust predictions under many iterations, we introduce a novel timescale-based update method, where a short-timestep update of each variable is computed by rescaling the predicted change over a longer timestep equal to its characteristic variation timescale. In one-zone collapse calculations, the results from the timescale-based method agree well with traditional numerical integration even with many iterations at a timestep as short as 10^{-4} of the free-fall time. This proof-of-concept study suggests the potential for neural network-based chemical emulators to accelerate hydrodynamic simulations of star formation.

Keywords: Population III stars (1285) — Neural networks (1933) — Star formation (1569) — Chemical reaction network models (2237) — Chemical abundances (224)

1. INTRODUCTION

In the Universe, gas collapses under gravity to form stars, which then disperse their material back into the interstellar medium via stellar winds and supernovae explosions. Over cosmic time-scales, this cycle has been repeated, gradually enriching the gas with metals produced in stellar interiors. Therefore, elucidating the physical properties and formation mechanisms of the first-generation stars, known as Population III (Pop III) stars, which emerged from primordial, metal-free gas at the onset of this cosmic cycle, is a fundamental challenge in modern astrophysics (for a recent review, see R. S. Klessen & S. C. O. Glover 2023). To gain a comprehensive understanding of Pop III star formation, it is essential to combine hydrodynamical simulations with detailed thermochemical evolution calculations (e.g., T. Abel et al. 2002; V. Bromm et al. 2002; N. Yoshida et al.

2008; T. Hosokawa et al. 2011; A. Stacy et al. 2012; H. Susa 2013; K. Sugimura et al. 2020).

However, modeling the thermochemical evolution involved in the formation of Pop III stars is computationally challenging. These calculations require solving stiff differential equations, which are often handled using implicit methods involving iterative solvers (e.g., K. Omukai 2001). As the stiffness increases, especially in high-density environments, the number of iterations needed for implicit updates can grow substantially, leading to a high computational cost. Furthermore, the number of iterations differs across cells, resulting in load imbalances that reduce parallel efficiency in large-scale simulations. When accounting for metal-enriched environments with more complex chemical networks, the computational difficulty becomes even more severe.

In recent years, machine learning (ML) using neural networks (NNs) has demonstrated its usefulness in wide scientific applications, including the solution of differential equations (L. M. Navarro et al. 2023). ML has the potential to reduce computational costs, as it can in-

fer solutions quickly and with fixed computational time once a model has been trained. Therefore, it is promising to construct emulators that accurately reproduce thermochemical evolution while avoiding the computational bottlenecks associated with implicit solvers.

A growing number of studies have been exploring the application of ML to emulate thermochemical evolution. After the seminal work in this direction by T. Grassi et al. (2011), dimensionality reduction techniques using autoencoders have been widely studied (J. Holdship et al. 2021; T. Grassi et al. 2022; I. Sulzer & T. Buck 2023; S. Maes et al. 2024). In related fields, ML has also been studied to improve the interpretation of ISM observations (D. de Mijolla et al. 2019; J. Heyl et al. 2023; P. Palud et al. 2023) and to model networks of nuclear reactions inside stars (A. Grichener et al. 2025).

Yet, the above autoencoder-based ML methods have been applied to limited situations: J. Holdship et al. (2021) developed an emulator for a fixed time interval; T. Grassi et al. (2022) and I. Sulzer & T. Buck (2023) constructed models for fixed density and temperature; and the model by S. Maes et al. (2024) is specialized for a one-dimensional model of AGB outflows. None of these approaches is suitable for modeling chemical evolution during star formation, where physical states and timescales vary widely.

Recently, L. Branca and A. Pallottini employed a physics-informed neural network (PINN) (M. Raissi et al. 2019) in L. Branca & A. Pallottini (2023), and later adopted deep operator network (DeepONet) (L. Lu et al. 2021a) in L. Branca & A. Pallottini (2024) to model the evolution of the interstellar medium (ISM) in a more general setup. The latter study achieved higher accuracy than the former, reporting both accurate predictions and a speed-up of up to 128 times compared to traditional methods.

However, P. van de Bor et al. (2025) found that the method presented in L. Branca & A. Pallottini (2024) is prone to instability due to the accumulation of prediction errors. The problem of iterative use of emulators has been recognized and partially addressed in the context of autoencoder-based methods. This issue has been mitigated either by injecting Gaussian noise during training (J. Holdship et al. 2021) or by training the iterative updates themselves (S. Maes et al. 2024). Moreover, no solution has yet been proposed for the method of L. Branca & A. Pallottini (2024), even though numerous iterations are inevitable when applying ML methods to hydrodynamic simulations.

Moreover, before applying the method of L. Branca & A. Pallottini (2024) to the case of star formation, another major challenge remains. While their model is not

constrained by the aforementioned limitation of previous autoencoder-based ML methods (e.g., J. Holdship et al. 2021; T. Grassi et al. 2022; I. Sulzer & T. Buck 2023; S. Maes et al. 2024), it still covers only low-density regimes typical of the ISM. To fully capture the star formation process, emulators must operate over a much wider density range, extending into the high-density protostellar regime.

The objective of this study is to take a first step toward fast and accurate emulation of thermochemical evolution in the star formation process using NNs. To this end, we extend the method of L. Branca & A. Pallottini (2024) in two directions.

First, we develop NN models that emulate the thermochemical evolution of gas during Pop III star formation, ranging from the low-density regime at the onset of gravitational collapse to the high-density regime associated with protostar formation. To address the difficulty of training NNs over the extremely wide density range encountered in star formation, we divide the full range into multiple subregions and train a separate NN in each subregion.

Second, we develop a new update method that ensures robust evolution under iteration of short-timestep predictions. In this method, each variable is updated by rescaling its predicted change over a characteristic timescale of significant variation if the timestep is so short that the physical change over the step is smaller than the typical prediction error. The characteristic timescale is estimated by auxiliary NNs.

In this proof-of-concept study, we aim to demonstrate that ML methods can be applied to model the thermochemical evolution during star formation. Therefore, we focus on the relatively simple case of metal-free, radiation-free primordial gas, and demonstrate the feasibility of using ML to emulate thermochemical evolution under these conditions. In the future, we also intend to extend this framework to more complex chemical networks that include metals and radiation.

This paper is organized as follows. In Section 2, we describe the basic equations for the thermochemical evolution and our NN methods to emulate the evolution. In Section 3, we present the results of emulation. Section 4 evaluates the acceleration achieved by NNs and compares our results with previous studies. Finally, in Section 5, we summarize our findings and outline future directions.

Throughout this paper, we use \log to denote \log_{10} for brevity.

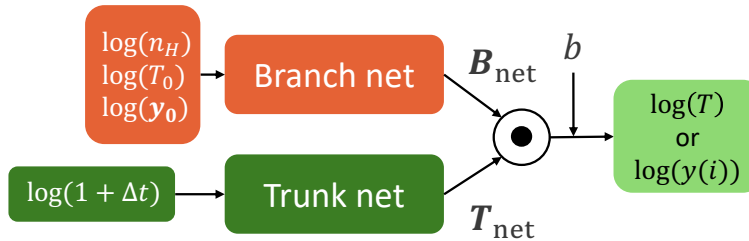


Figure 1. Schematic diagram of DeepONet, which consists of two networks: the branch net and the trunk net. The branch net receives the hydrogen nucleus number density n_{H} , the initial temperature T_0 , and the initial chemical abundances \mathbf{y}_0 as input, in the form of $\log(n_{\text{H}}/\text{cm}^{-3})$, $\log(T_0/\text{K})$, and $\log(\mathbf{y}_0)$, respectively. The trunk net takes the timestep Δt as input in the form of $\log(1 + \Delta t/\text{sec})$. The final output is computed as the inner product of the branch net output \mathbf{B}_{net} and the trunk net output \mathbf{T}_{net} , plus a bias term b : $\mathbf{B}_{\text{net}} \cdot \mathbf{T}_{\text{net}} + b$. A separate DeepONet model is constructed for each target variable, which is either the updated temperature T in the form of $\log(T/\text{K})$ or the updated chemical abundance of the i -th species $y(i)$ in the form of $\log(y(i))$.

2. METHODS

2.1. Basic Equations

We investigate the thermochemical evolution of primordial gas clouds during Pop III star formation. To model this evolution, we solve a set of ordinary differential equations (ODEs) governing the time evolution of the gas temperature and the abundances of key chemical species.

Our chemical model is based on K. Sugimura et al. (2020, 2023), with additional high-density reactions (K. E. Sadanari et al. 2021). The model tracks six chemical species: H, H₂, e⁻, H⁺, H⁻, and H₂⁺, which are involved in a network of 18 chemical reactions (see Appendix A for details). We focus on the pre-protostellar collapse phase and assume no external radiation field.

Heating and cooling processes are modeled as follows. For line cooling, we consider H₂ line cooling and Ly α cooling. We compute the H₂ line cooling rate using the optically thin cooling function from S. C. O. Glover (2015) with an average line escape probability obtained in H. Fukushima et al. (2018). For continuum cooling, we consider H free-bound emission, H⁻ free-bound and free-free emission, H free-free emission, H₂-H₂ collision-induced emission (CIE), and H₂-He CIE. We calculate the cooling rate using the optical depth estimated with the Jeans length (see K. E. I. Tanaka & K. Omukai 2014, for details), with continuum opacity from R. Matsukoba et al. (2019). Chemical heating and cooling are also included.

To simplify the model, we track only hydrogen-bearing species. Although deuterium chemistry, particularly HD cooling, plays a crucial role in the formation of low-mass Pop III stars (T. Nagakura & K. Omukai 2005), we focus on the typical high-mass case and omit deuterium. We also neglect lithium chemistry, which does not affect thermal evolution but can alter the ionization

fraction and, consequently, non-ideal magnetohydrodynamic (MHD) effects in magnetized environments (D. Nakauchi et al. 2019; K. E. Sadanari et al. 2023). Helium is assumed to remain fully neutral, with a fixed abundance of $y_{\text{He}} = n_{\text{He}}/n_{\text{H}} = 9.7 \times 10^{-2}$, where n_{H} and n_{He} are the number densities of hydrogen and helium nuclei, respectively.

The basic equations for the time evolution of the chemical abundances and gas temperature are given by

$$\dot{y}(i) = \sum_j A_{ij}(n_{\text{H}}, T, \mathbf{y}), \quad (1)$$

$$n_{\text{H}} c_v \dot{T} = \Gamma(n_{\text{H}}, T, \mathbf{y}) - \Lambda(n_{\text{H}}, T, \mathbf{y}), \quad (2)$$

where \mathbf{y} is the vector of chemical abundances, and each abundance $y(i)$ is defined as $y(i) = n(i)/n_{\text{H}}$, with $n(i)$ being the number density of species i . The index i runs from 1 to 6 and corresponds to H, H₂, e⁻, H⁺, H⁻, and H₂⁺, respectively. Note that $n(1) = n(\text{H})$ denotes the number density of neutral hydrogen, which is different from n_{H} , the total number density of hydrogen nuclei. A_{ij} denotes the contribution of reaction j to $\dot{y}(i)$. The gas temperature is denoted by T , and c_v is the specific heat at constant volume per hydrogen nucleus, depending on both T and \mathbf{y} (K. Omukai & R. Nishi 1998). The functions $\Gamma(n_{\text{H}}, T, \mathbf{y})$ and $\Lambda(n_{\text{H}}, T, \mathbf{y})$ represent the heating and cooling rates, respectively. Compressional heating is excluded from Γ , as it is treated separately by operator splitting when gas dynamics is included.

In this work, we mainly focus on the thermochemical evolution at densities below $n_{\text{H}} = 10^{18} \text{ cm}^{-3}$, where non-equilibrium chemistry and radiative (line and continuum) cooling are essential (K. Omukai 2001). At higher densities, we do not need to solve Eqs. (1) and (2) explicitly because reaction timescales become so short that chemical equilibrium is a good approximation, and the gas becomes so optically thick that radiative cooling is negligible and the gas can be treated as adiabatic. In

this regime, the thermal and chemical state can be obtained from the Saha equation (M. N. Saha 1920) with a given total energy. Accordingly, for $n_{\text{H}} > 10^{18} \text{ cm}^{-3}$, instead of constructing a chemical emulator, we model the thermochemical evolution by interpolating a precalculated table of temperature and equilibrium abundances as a function of density and total energy (see Appendix B for details). This method can significantly reduce the computational cost compared with conventional numerical integration.

We train the NN emulator using a set of physical states that broadly cover the thermal and chemical trajectories during Pop III star formation, which are obtained from one-zone calculations of a gravitationally collapsing gas cloud. The same trajectories are used to validate the emulator after training. The one-zone model follows the evolution of the central core, assuming free-fall collapse, $\dot{n}_{\text{H}} = n_{\text{H}}/t_{\text{ff}}$, where the free-fall time is given by $t_{\text{ff}} = (3\pi/(32G\rho))^{1/2}$, with the mass density $\rho = (1 + 4y_{\text{He}})n_{\text{H}}m_{\text{H}}$ and the hydrogen mass m_{H} .

The calculation starts from conditions corresponding to Pop III star formation at $z = 16$ (K. Sugimura et al. 2014): $n_{\text{H}} = 4.5 \times 10^{-3} \text{ cm}^{-3}$, $T = 21 \text{ K}$, $y(e^-) = 3.7 \times 10^{-4}$, and $y(\text{H}_2) = 2 \times 10^{-6}$. We evolve the system until $n_{\text{H}} = 10^{18} \text{ cm}^{-3}$, below which the chemical evolution must be treated in non-equilibrium. At each timestep, we (i) update T and \mathbf{y} , (ii) add compressional heating $\Gamma_{\text{comp}} = (\sum_i y(i) + y_{\text{He}})k_{\text{B}}\dot{n}_{\text{H}}T$, where k_{B} is the Boltzmann constant, and (iii) increase the density.

In this work, we test four timestep sizes: $\Delta t = 10^{-1}$, 10^{-2} , 10^{-3} , and $10^{-4} t_{\text{ff}}$. In a one-zone model, the relevant timescales are the free-fall time t_{ff} and the thermal and chemical timescales. However, in multi-zone hydrodynamic simulations, the timestep can be much shorter than these timescales, for instance, when the Courant condition imposed by small adaptive-mesh-refinement cells limits the timestep for the entire computational domain (e.g., K. Sugimura et al. 2020, 2023). In cases with small timesteps, such as $\Delta t \ll t_{\text{ff}}$, the physical change per step can be comparable to or even smaller than the typical NN prediction error. Consequently, iterative NN updates can be dominated by the error and result in unphysical predictions (P. van de Bor et al. 2025). We address this problem by introducing a new method in Section 2.3.

2.2. Neural Network for Emulating Thermal and Chemical Evolution: DeepONet

We emulate the thermochemical evolution given by Eqs.(1) and (2) employing DeepONet. DeepONet is a NN architecture originally developed to learn nonlinear operators and has recently been applied to solving dif-

ferential equations. In astrophysics, L. Branca & A. Pallottini (2024) successfully used DeepONet to model the thermochemical evolution of the ISM. We follow their methodology and adapt the network to the context of Pop III star formation. Our implementation uses the DeepXDE library (L. Lu et al. 2021b) built on the TensorFlow framework (M. Abadi et al. 2015), which includes various DeepONet-related modules.

The overall structure of DeepONet is illustrated in Figure 1. A key feature of DeepONet is that it consists of two separate subnetworks: *the branch net* and *the trunk net*. Each is a standard feedforward NN with fully-connected layers, where each layer performs the transformation:

$$\phi_l = \sigma(\phi_{l-1}\mathbf{W}_l + \mathbf{b}_l) \quad (l = 1, 2, \dots, N_l), \quad (3)$$

where $\phi_l \in \mathbb{R}^{d_l}$, $\mathbf{W}_l \in \mathbb{R}^{d_{l-1} \times d_l}$, and $\mathbf{b}_l \in \mathbb{R}^{d_l}$ are the output, the weight matrix and bias vector of the l -th layer, respectively, and σ is the activation function. The input vector $\mathbf{X} \in \mathbb{R}^s$ of dimension s corresponds to the input ϕ_0 , with $d_0 = s$. The number of neurons in each layer is denoted by d_l , and N_l is the total number of layers. We adopt the Rectified Linear Unit (ReLU) function (X. Glorot et al. 2011) $\text{ReLU}(x) = \max(0, x)$ as the activation function $\sigma(x)$. We do not apply an activation function in the final layer of the branch net. In our setup, both the branch net and the trunk net consist of 10 fully-connected layers, each with 128 neurons (i.e., $N_l = 10$ and $d_l = 128$ for $1 \leq l \leq N_l$).

The outputs of the branch net and the trunk net are vectors, denoted by \mathbf{B}_{net} and \mathbf{T}_{net} , respectively. The final output of DeepONet is a scalar Y given by:

$$Y = \mathbf{B}_{\text{net}} \cdot \mathbf{T}_{\text{net}} + b, \quad (4)$$

where $b \in \mathbb{R}$ is a learnable bias parameter.

This structure enables the DeepONet architecture to reduce generalization error by distinguishing between physically distinct variables, in contrast to a standard fully-connected NN that treats all inputs as a single, undifferentiated vector (L. Lu et al. 2021a).

The branch net receives the hydrogen number density n_{H} , the initial temperature T_0 , and the initial chemical abundances \mathbf{y}_0 as inputs in the form of $\log(n_{\text{H}}/\text{cm}^{-3})$, $\log(T_0/\text{K})$, and $\log(\mathbf{y}_0)$, respectively. The trunk net takes the timestep Δt in the form of $\log(1 + \Delta t/\text{sec})$. The output Y is either the temperature ($\log(T/\text{K})$) or the abundance of the i -th chemical species ($\log(y(i))$) after evolution over Δt from the initial state. We train a separate DeepONet model for each target variable, resulting in a total of seven models for the temperature and the six chemical species.

We define the total loss function as

$$L = \text{MSE} + L1 + L2, \quad (5)$$

and train the DeepONet models to minimize this function. Here, the Mean Squared Error (MSE) is defined as

$$\text{MSE} = \frac{1}{N_{\text{batch}}} \sum_{n=1}^{N_{\text{batch}}} |Y_{n,\text{true}} - Y_{n,\text{pred}}|^2, \quad (6)$$

where $Y_{n,\text{true}}$ and $Y_{n,\text{pred}}$ are the true results obtained from numerical integration and DeepONet predictions, respectively, for the n -th training sample, and $N_{\text{batch}} = 10^5$ denotes the batch size used to divide the training data. To prevent overfitting, we also include both L1 and L2 regularization terms (R. Tibshirani 1996; A. E. Hoerl & R. W. Kennard 1970a,b):

$$L1 = \lambda_1 \sum_i |w_i|, \quad L2 = \lambda_2 \sum_i w_i^2, \quad (7)$$

where w_i denotes each element of the weight matrices and bias vectors in Eq.(3) and the bias parameter in Eq.(4), and the regularization coefficients are set to $\lambda_1 = \lambda_2 = 10^{-8}$.

The DeepONet models are trained using the Adam optimizer (D. P. Kingma & J. Ba 2014). During each epoch, which corresponds to training over the entire dataset of 5.12×10^8 samples (see Section 2.4), the model parameters are updated after every batch of $N_{\text{batch}} = 10^5$ samples, resulting in 5120 iterations per epoch. We start the training with an initial learning rate of 10^{-3} . The loss function is evaluated every 640 iterations, and the learning rate is halved if no improvement is observed for ten consecutive evaluations (i.e., after 6400 iterations). Note that 640 iterations are much shorter than one epoch. Through multiple trials with different learning-rate scheduling, we empirically found that frequent monitoring is required to achieve stable training.

The range of densities considered is $10^{-3} \text{ cm}^{-3} \leq n_{\text{H}} \leq 10^{18} \text{ cm}^{-3}$ and spans more than 20 orders of magnitude. As a single DeepONet model cannot learn the entire range with sufficient accuracy, we partition it into five subranges: 10^{-3} – 10^4 , 10^4 – 10^8 , 10^8 – 10^{12} , 10^{12} – 10^{15} , and 10^{15} – 10^{18} cm^{-3} ; hereafter, Regions 0, 1, 2, 3, and 4, respectively. We construct a separate DeepONet model for each of these regions.

2.3. Timescale-based Method for Robust Iterative Predictions

2.3.1. Basic scheme

Time integration with iterative NN updates can produce unphysical solutions, for instance, through the accumulation of prediction errors (P. van de Bor et al.

2025). To mitigate this, we introduce a simple yet effective method that ensures robust predictions under iterative updates.

Before presenting our method, we briefly explain the mechanism that leads to unphysical solutions. Consider the evolution of a variable under repeated NN predictions. If the timestep is very short, the physical change over that step can be smaller than the prediction error. In such a case, the time variation is dominated by the error rather than by the physical evolution, and iterating such updates drives the solution away from the physical one.

To address this issue, we propose a modified update method based on a characteristic timescale for significant variation. For a physical quantity x , we choose a dimensionless parameter ϵ significantly smaller than the typical relative error of DeepONet predictions. Then, we define the characteristic timescale τ_ϵ as the interval over which the physical evolution changes x by a fraction ϵ , i.e., $|\Delta x(\tau_\epsilon)| = \epsilon |x|$.

Finally, we define the change in a quantity x over a timestep Δt as

$$\Delta x(\Delta t) = \begin{cases} \frac{\Delta t}{\tau_\epsilon} \Delta x_{\text{pred}}(\tau_\epsilon), & \Delta t < \tau_\epsilon, \\ \Delta x_{\text{pred}}(\Delta t), & \Delta t \geq \tau_\epsilon, \end{cases} \quad (8)$$

where $\Delta x_{\text{pred}}(\Delta t')$ is the change predicted by DeepONet over an interval $\Delta t'$. Hereafter, we call this method the *timescale-based method*.

When $\Delta t < \tau_\epsilon$, this method replaces the short-timestep prediction $\Delta x_{\text{pred}}(\Delta t)$, dominated by the prediction error, with a scaled version of a longer-timestep prediction $(\Delta t/\tau_\epsilon) \Delta x_{\text{pred}}(\tau_\epsilon)$, dominated by physical evolution. On the other hand, when $\Delta t \geq \tau_\epsilon$, the method simply returns the DeepONet prediction $\Delta x_{\text{pred}}(\Delta t)$ because the prediction error is subdominant. As a result, the prediction error is always smaller than the physical evolution at each update, enabling robust predictions even under short-timestep iterations.

In Eq. (8), we cap the value of τ_ϵ at the maximum timestep learned by DeepONet, Δt_{max} , since NNs generally make unreliable predictions outside the learned region. In addition, we enforce the hydrogen nucleus conservation and charge neutrality conditions after each update to improve the stability of evolution.

In general, the characteristic timescale τ_ϵ differs for each target variable. Since our DeepONet framework uses a separate model for each variable, each variable is updated with its own DeepONet model and τ_ϵ in Eq. (8).

2.3.2. Neural Network for Estimating Characteristic Timescales: Deep Galerkin Method

Naively, one may think τ_ϵ can be obtained by using the instantaneous time derivative \dot{x} as $\tau_\epsilon = \epsilon x / \dot{x}$. However, due to the stiffness of the system, τ_ϵ obtained in this way can be orders-of-magnitude smaller than the actual time required for the fractional change of x to reach ϵ . Alternatively, τ_ϵ can be obtained by numerical integration of the ODEs until the change in x reaches $\pm \epsilon x$. However, such a procedure is computationally expensive.

To reduce the computational cost of estimating τ_ϵ , we introduce new NNs in addition to the DeepONet models described in Section 2.2. Here, we construct Deep Galerkin Method (DGM)-based NNs (J. Sirignano & K. Spiliopoulos 2018) to estimate τ_ϵ , using PyTorch (A. Paszke et al. 2019). The DGM architecture, which has been applied to modeling the ISM (L. Branca & A. Pallottini 2023), is suited to problems where the output changes sharply in response to the input, such as estimating τ_ϵ for a given chemical and thermal state.

Following L. Branca & A. Pallottini (2023), the architecture of the DGM network is defined as (see also J. Sirignano & K. Spiliopoulos 2018):

$$\phi_0 = \sigma(\mathbf{X}U_0 + \mathbf{b}_0), \quad (9)$$

$$\mathbf{Z}_l = \sigma\left(\mathbf{X}U_l^{(z)} + \phi_{l-1}\mathbf{W}_l^{(z)} + \mathbf{b}_l^{(z)}\right), \quad (10)$$

$$\mathbf{G}_l = \sigma\left(\mathbf{X}U_l^{(g)} + \phi_{l-1}\mathbf{W}_l^{(g)} + \mathbf{b}_l^{(g)}\right), \quad (11)$$

$$\mathbf{R}_l = \sigma\left(\mathbf{X}U_l^{(r)} + \phi_{l-1}\mathbf{W}_l^{(r)} + \mathbf{b}_l^{(r)}\right), \quad (12)$$

$$\mathbf{H}_l = \sigma\left(\mathbf{X}U_l^{(h)} + (\phi_{l-1} \odot \mathbf{R}_l)\mathbf{W}_l^{(h)} + \mathbf{b}_l^{(h)}\right), \quad (13)$$

$$\phi_l = (1 - \mathbf{G}_l) \odot \mathbf{H}_l + \mathbf{Z}_l \odot \phi_{l-1}, \quad (14)$$

$$\mathbf{Y} = \phi_{N_l}\mathbf{W} + \mathbf{b}, \quad (15)$$

where the intermediate DGM layers ($l = 1, 2, \dots, N_l$ with N_l the number of DGM layers) are sandwiched by the fully-connected first and last layers. Each DGM layer receives both the input vector $\mathbf{X} \in \mathbb{R}^s$ and the output of the previous layer ϕ_{l-1} . At each DGM layer, intermediate states \mathbf{Z}_l , \mathbf{G}_l , \mathbf{R}_l , and $\mathbf{H}_l \in \mathbb{R}^{d_l}$ are computed and then combined to yield the layer output $\phi_l \in \mathbb{R}^{d_l}$ (here, \odot denotes the Hadamard product). For each of $(*) \in \{z, g, r, h\}$, $U_l^{(*)} \in \mathbb{R}^{s \times d_l}$, $\mathbf{W}_l^{(*)} \in \mathbb{R}^{d_{l-1} \times d_l}$, $\mathbf{b}_l^{(*)} \in \mathbb{R}^{d_l}$ are the weights for \mathbf{X} , the weights for ϕ_{l-1} , and the biases, respectively. Finally, the last layer yields the output vector \mathbf{Y} , without applying any activation function. Unlike conventional fully-connected layers, each DGM layer consists of repeated element-wise multiplications involving nonlinear transformations of the input, making DGM networks suited

to emulating complex and rapidly varying functions (J. Sirignano & K. Spiliopoulos 2018).

The input is the same as that of the branch net of DeepONet (Section 2.2), i.e, a vector of the density and the initial temperature and abundances in the form of $\log(n_{\text{H}}/\text{cm}^{-3})$, $\log(T_0/\text{K})$, and $\log(\mathbf{y}_0)$. The output is a vector of the timescales τ_ϵ for the temperature and six chemical abundances. Unlike DeepONet, a single DGM model outputs all target variables simultaneously. We choose the sigmoid function $\text{sigmoid}(x) = (1 + e^{-x})^{-1}$ as the activation function $\sigma(x)$. In our setup, the DGM network consists of 10 DGM layers, each with 128 neurons.

To facilitate learning, instead of estimating τ_ϵ directly, we introduce the auxiliary variable

$$Y_\tau = \begin{cases} \log\left(1 + \epsilon \frac{t_{\text{ff}}}{\tau_\epsilon}\right), & \Delta x > 0, \\ -\log\left(1 + \epsilon \frac{t_{\text{ff}}}{\tau_\epsilon}\right), & \Delta x < 0. \end{cases} \quad (16)$$

For $\epsilon t_{\text{ff}}/\tau_\epsilon \ll 1$ we have $Y_\tau \simeq \pm \epsilon t_{\text{ff}}/\tau_\epsilon$, corresponding to the normalized time derivative \dot{x}/x . When $\epsilon t_{\text{ff}}/\tau_\epsilon \gg 1$, the logarithmic form in Eq. (16) bounds Y_τ and avoids numerical difficulties caused by very large $1/\tau_\epsilon$.

For the DGM network, we extend the loss function of DeepONet (Eq. (5)) to handle multiple outputs. Specifically, we modify the MSE of DeepONet (Eq. (6)) by summing over all output components:

$$\text{MSE}_\tau = \sum_{i=0}^6 \left(\frac{1}{N_{\text{batch}}} \sum_{n=1}^{N_{\text{batch}}} |Y_{\tau,i,n,\text{true}} - Y_{\tau,i,n,\text{pred}}|^2 \right), \quad (17)$$

where i corresponds to the seven components (temperature and six chemical species), and $Y_{\tau,i,n,\text{true}}$ and $Y_{\tau,i,n,\text{pred}}$ denote the true and estimated values of Y_τ for the i -th component for the n -th training sample, respectively. In DGM network training, we also take $N_{\text{batch}} = 10^5$. We add L1 and L2 regularization (Eq. (7)) on all weights and biases, with $\lambda_1 = 10^{-6}$ and $\lambda_2 = 10^{-7}$. The total loss is then:

$$L_\tau = \text{MSE}_\tau + L1 + L2. \quad (18)$$

Finally, we split the density range into the same five regions used for DeepONet (Section 2.2) and train a separate DGM model in each region.

2.4. Dataset Generation

Here, we explain how we generate training datasets for the two types of NNs, the DeepONet (Section 2.2) and DGM (Section 2.3.2) models. The ranges of temperature and chemical abundances in the datasets are designed to

sufficiently cover the one-zone thermochemical evolution paths for Pop III star formation (Section 2.1).

We generate datasets by numerically integrating the thermochemical evolution equations (Eqs. (1) and (2)) from a given initial state. To ensure numerical stability and accuracy, the equations are integrated using a fully-implicit scheme with adaptive substepping. Although the fully-implicit scheme is numerically stable, the errors can become non-negligible when the variations in T or $y(i)$ are large. Therefore, the timestep is subdivided so that the relative changes in T and $y(i)$ remain within 10% per substep. We have confirmed that further reduction of the substep size (below 10%) does not significantly affect the results. Hence, we adopt the 10% substepping criterion throughout this work.

For both the DeepONet and DGM models, the ranges of the input parameters for each density region (see Section 2.2) are summarized in Table 1. To generate initial states, we first sample the temperature and chemical abundances uniformly within the ranges shown in Table 1. We then adjust the abundances to enforce hydrogen-nucleus conservation and overall charge neutrality. Because this procedure can shift the abundances outside the original parameter space, primarily toward higher values, the table should be understood as defining the original sampling range, while the actual parameter space may be somewhat broader.

For the DeepONet models, we also randomly sample the timestep parameter $\log(1 + \Delta t/\text{sec})$ between 0 and $\log(1 + \Delta t_{\text{max}}/\text{sec})$, with $\Delta t_{\text{max}} = 10^{0.5} t_{\text{ff}}$, and evolve each initial state for Δt . Each training dataset contains 5.12×10^8 samples. For validation, an additional set of 5,120 samples is created. Generating the dataset required roughly 200 CPUhrs per region.

For the DGM models, given that the prediction errors are typically less than 5% (or mostly less than 10%; see Table 2 in Section 3.1.1 below), we compute τ_ϵ for $\epsilon = 0.1$. We have confirmed that the exact value of ϵ , and hence τ_ϵ , does not affect the results significantly by performing test computations with doubled τ_ϵ . In obtaining τ_ϵ , we evolve each initial state while recording the time when the relative change of each variable reaches 10%. The size of the training dataset and an additional validation dataset for each region is again 5.12×10^8 and 5,120 samples, respectively. The dataset generation time for each region was approximately 170 CPUhrs.

Training was conducted on NVIDIA A100 GPUs (40 GB). The DeepONet models were trained for 50 epochs, requiring about 1.67 GPUhrs per variable (temperature or abundance), leading to a total of 11.7 GPUhrs per

region. The DGM models were trained for 100 epochs and required approximately 15.2 GPUhrs per region.

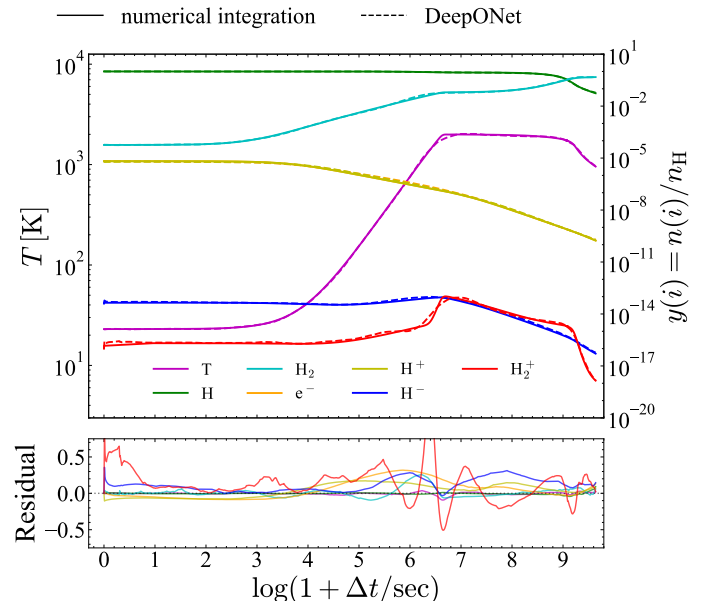


Figure 2. Single-step DeepONet predictions of the thermal and chemical evolution for a fixed hydrogen number density of $n_{\text{H}} = 10^{12} \text{ cm}^{-3}$. The top panel compares the DeepONet predictions (dashed) with the ground-truth results from numerical integrations (solid). The bottom panel plots the corresponding residual errors normalized by the ground-truth values, i.e., $(T_{\text{pred}} - T_{\text{true}})/T_{\text{true}}$ or $(y_{\text{pred}}(i) - y_{\text{true}}(i))/y_{\text{true}}(i)$, where the subscripts “pred” and “true” denote the DeepONet and ground-truth values, respectively. The horizontal axis represents the transformed timestep, $\log(1 + \Delta t/\text{sec})$. The DeepONet predictions almost perfectly reproduce the ground-truth results. The variables are color-coded as follows: T (magenta); $y(\text{H})$ (green); $y(\text{H}_2)$ (cyan); $y(\text{e}^-)$ (orange); $y(\text{H}^+)$ (yellow); $y(\text{H}^-)$ (blue); and $y(\text{H}_2^+)$ (red). Note that the curves for $y(\text{e}^-)$ are nearly invisible because they almost completely coincide with those for $y(\text{H}^+)$.

3. RESULTS

3.1. Performance of DeepONet-based Emulator

Here, we evaluate the performance of the DeepONet-based emulator (Section 2.2) in two cases: single-step evolution from an initial state (Section 3.1.1) and a one-zone collapse calculation (Section 3.1.2). These tests demonstrate that the emulator successfully learns the thermochemical evolution over the wide range of densities relevant to Pop III star formation.

3.1.1. Single-step predictions of thermal and chemical evolution at a fixed density

Here, we demonstrate that our DeepONet models can accurately predict the thermochemical evolution of pri-

Table 1. Parameter ranges for training dataset in each density region

	Region 0		Region 1		Region 2		Region 3		Region 4	
	min	max								
$\log(n_{\text{H}}/\text{cm}^{-3})$	-3	4	4	8	8	12	12	15	15	18
$\log(T/\text{K})$	1.3	4.5	1.3	4.5	1.3	4.0	1.3	4.0	1.3	4.0
$\log(y(\text{H}))$	-6	0	-6	0	-6	0	-6	0	-6	0
$\log(y(\text{H}_2))$	-8	-0.3	-6	-0.3	-6	-0.3	-6	-0.3	-6	-0.3
$\log(y(\text{e}^-))$	-10	-4	-10	-4	-12	-6	-14	-8	-15	-9
$\log(y(\text{H}^+))$	-10	-4	-10	-4	-12	-6	-14	-8	-15	-9
$\log(y(\text{H}^-))$	-19	-13	-20	-14	-21	-15	-21	-15	-22	-16
$\log(y(\text{H}_2^+))$	-19	-13	-20	-14	-21	-15	-21	-15	-22	-16

NOTE— The value of 1.3 for the lower bound of temperature corresponds to $\log(20)$, i.e., a temperature of $T = 20$ K. The value of -0.3 for the upper bound of H_2 abundance corresponds to $\log(0.5)$, which reflects the constraint that $y(\text{H}_2)$ cannot exceed 0.5.

Table 2. Fraction of predictions with relative errors Δ_Y below 5% and 10% for each variable in each density region.

Δ_Y	Region 0		Region 1		Region 2		Region 3		Region 4	
	< 5%	< 10%	< 5%	< 10%	< 5%	< 10%	< 5%	< 10%	< 5%	< 10%
T	97%	99%	98%	100%	99%	100%	100%	100%	100%	100%
H	100%	100%	99%	100%	99%	100%	97%	99%	92%	98%
H_2	94%	97%	84%	91%	91%	96%	94%	99%	95%	100%
e^-	97%	99%	91%	97%	87%	95%	91%	97%	72%	87%
H^+	96%	99%	90%	97%	84%	94%	91%	97%	74%	88%
H^-	66%	86%	64%	87%	72%	90%	77%	93%	68%	86%
H_2^+	52%	74%	48%	74%	49%	74%	49%	75%	53%	78%

NOTE— Each density region is defined as follows: Region 0 ($10^{-3} \leq n_{\text{H}}/\text{cm}^{-3} \leq 10^4$); Region 1 ($10^4 \leq n_{\text{H}}/\text{cm}^{-3} \leq 10^8$); Region 2 ($10^8 \leq n_{\text{H}}/\text{cm}^{-3} \leq 10^{12}$); Region 3 ($10^{12} \leq n_{\text{H}}/\text{cm}^{-3} \leq 10^{15}$); and Region 4 ($10^{15} \leq n_{\text{H}}/\text{cm}^{-3} \leq 10^{18}$).

mordial gas. We begin with an example of time evolution from a specific initial condition and then assess the distribution of prediction errors for a large sample of initial conditions.

Let us examine the time evolution at a fixed density of $n_{\text{H}} = 10^{12} \text{ cm}^{-3}$ starting from the following initial condition: $T = 23 \text{ K}$, $y(\text{H}_2) = 5.7 \times 10^{-5}$, $y(\text{H}^+) = 6.6 \times 10^{-6}$, $y(\text{H}^-) = 4.0 \times 10^{-14}$, and $y(\text{H}_2^+) = 1.0 \times 10^{-16}$, with $y(\text{H})$ and $y(\text{e}^-)$ determined to satisfy the hydrogen nucleus conservation and charge neutrality conditions. We examine single-step predictions over the timestep Δt , sampled logarithmically as $\log(1 + \Delta t/\text{sec}) = (i/1000) \log(1 + \Delta t_{\text{max}}/\text{sec})$ for $i = 1, 2, \dots, 1000$. Here, we employ the model for

Region 3, while the density $n_{\text{H}} = 10^{12} \text{ cm}^{-3}$ is located at the boundary of Regions 2 and 3 (see Table 1).

Note that the initial chemical abundances fall slightly outside the range of Region 3 in Table 1. We regard the examination of the emulator under this initial condition as a stringent quality test, which demonstrates the model’s flexibility beyond the training range of Table 1 and provides insights into possible overfitting.

Figure 2 presents the DeepONet predictions (dashed lines) together with the ground-truth numerical integration results (solid lines). The DeepONet model almost perfectly reproduces the highly nonlinear evolution: it captures the early chemical heating driven by H_2 formation for $3 < \log(1 + \Delta t/\text{sec}) < 7$, as well as the late-time H_2 cooling following further H_2 formation at

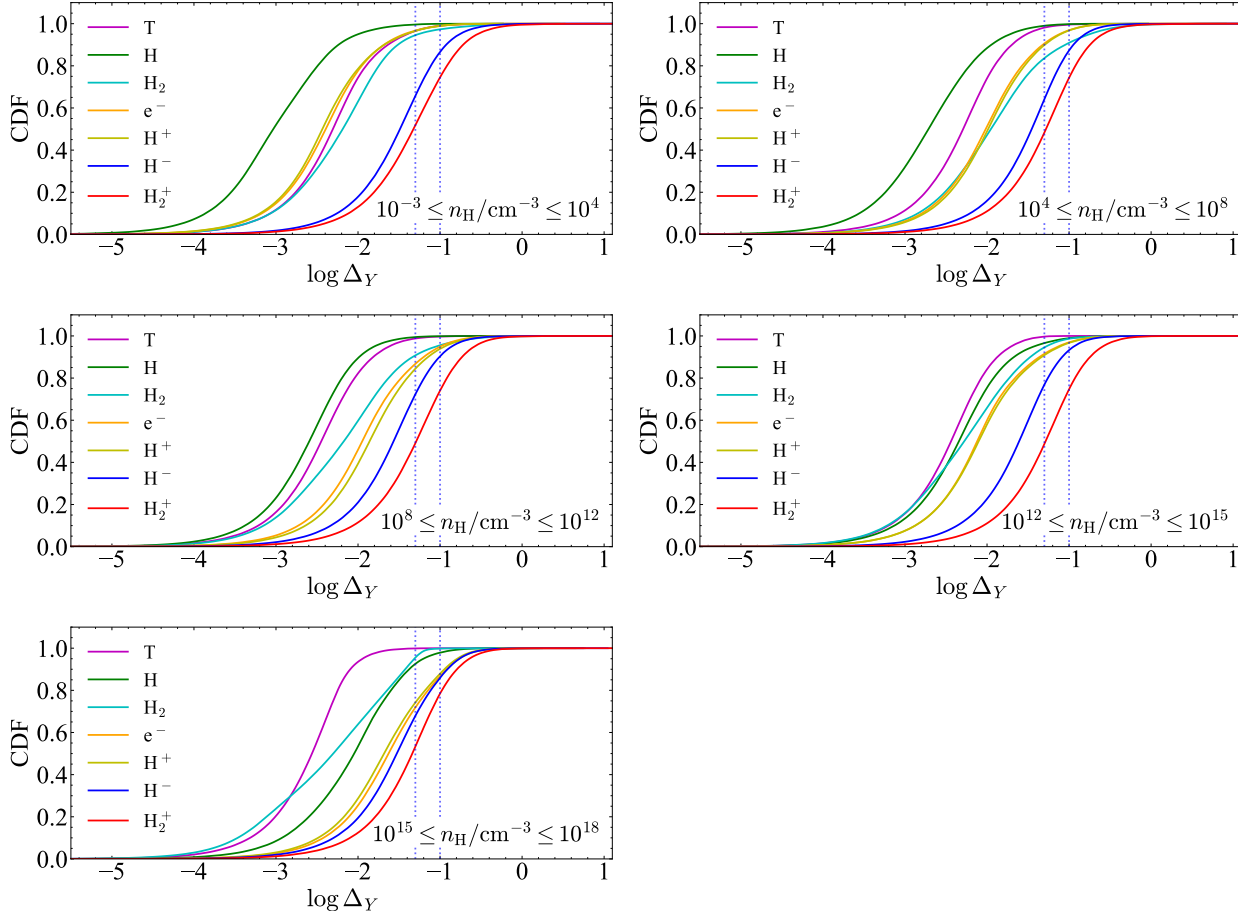


Figure 3. Cumulative distribution functions of the relative prediction errors of the DeepONet emulator for each density region. The horizontal axis shows the logarithm of relative error Δ_Y , defined in Eq. (19), and the vertical axis indicates the cumulative relative frequency. The two blue dotted vertical lines show $\Delta_Y = 0.05$ (left) and 0.1 (right). Each panel corresponds to a different density range: Region 0 ($10^{-3} \leq n_{\text{H}}/\text{cm}^{-3} \leq 10^4$, top left); Region 1 ($10^4 \leq n_{\text{H}}/\text{cm}^{-3} \leq 10^8$, top right); Region 2 ($10^8 \leq n_{\text{H}}/\text{cm}^{-3} \leq 10^{12}$, middle left); Region 3 ($10^{12} \leq n_{\text{H}}/\text{cm}^{-3} \leq 10^{15}$, middle right); and Region 4 ($10^{15} \leq n_{\text{H}}/\text{cm}^{-3} \leq 10^{18}$, bottom left). Colors are the same as in Figure 2.

$\log(1+\Delta t/\text{sec}) > 9$. Although the initial chemical abundances slightly exceed the range defined in Table 1, as mentioned before, the errors remain below 30% (except for the minor species H_2^+ , whose residual exceeds 50% around $\log(1+\Delta t/\text{sec}) \approx 6.5$, where the emulated curve is less sharp than the numerical-integration result), indicating that the model can emulate the evolution even when the input slightly exceeds the range defined in Table 1. We have also confirmed that the errors become smaller ($\lesssim 10\%$) for the initial conditions that fall within the range of Table 1. These results demonstrate that the model has successfully learned the underlying physical processes.

To assess the general accuracy of DeepONet predictions, we evaluate prediction errors using independent test datasets consisting of 5.12×10^5 samples that were not used in training or validation. The relative error Δ_Y

for each prediction is defined as

$$\Delta_Y = \left| \frac{10^{Y_{\text{pred}}} - 10^{Y_{\text{true}}}}{10^{Y_{\text{true}}}} \right|, \quad (19)$$

where Y is either $\log(T/\text{K})$ or $\log(y(i))$, and the subscripts “true” and “pred” denote the values from numerical integration and DeepONet prediction, respectively. The cumulative distribution function (CDF) of $\log(\Delta_Y)$ is shown in Figure 3 for each variable and each density region. The relative errors are typically smaller than $\Delta_Y = 0.05$ and in most cases smaller than $\Delta_Y = 0.1$.

Table 2 summarizes the fraction of predictions whose relative errors are below 5% and 10% for each variable in each density region. These fractions correspond to the cumulative relative frequency evaluated at $\Delta_Y = 0.05$ and 0.1 , respectively. Except for $y(\text{H}_2^+)$, more than $\sim 90\%$ of the predictions have errors smaller than 10%.

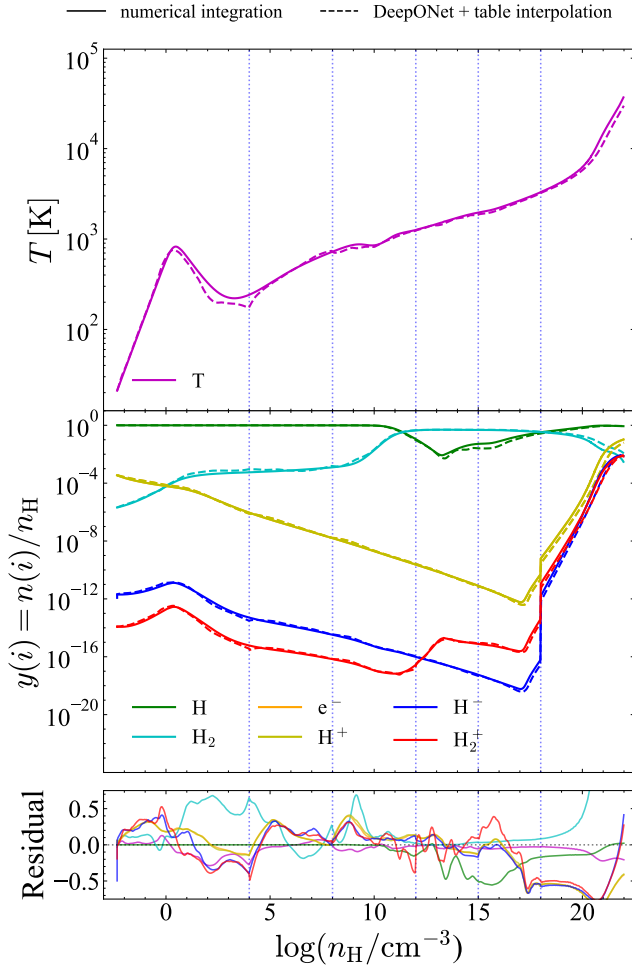


Figure 4. One-zone evolution with timestep $\Delta t = 10^{-1} t_{\text{ff}}$. The horizontal axis is the hydrogen number density n_{H} , corresponding to the time evolution during gravitational collapse. The top panel shows the temperature evolution, the middle panel shows the chemical evolution, and the bottom panel shows the residual errors. Blue dotted vertical lines indicate the boundaries between different density regions. Colors are the same as in Figure 2. The solid lines show the ground-truth numerical integration results, while the dashed lines show the DeepONet predictions for $n_{\text{H}} \leq 10^{18} \text{ cm}^{-3}$ and the results obtained by interpolating a precalculated table for $n_{\text{H}} \geq 10^{18} \text{ cm}^{-3}$ (see Appendix B). Note that the apparent jump in the abundances of e^- , H^+ , H^- , and H_2^+ at $n_{\text{H}} = 10^{18} \text{ cm}^{-3}$, arising due to the absence of inverse reactions in our chemical network, does not affect the thermal evolution (D. Nakauchi et al. 2019). The abundances of e^- and H^+ overlap almost completely with each other.

The relatively large error for $y(\text{H}_2^+)$ is expected, because this species is often extremely rare and its logarithmic value is sensitive to numerical noise. Nonetheless, because more than $\sim 75\%$ of the $y(\text{H}_2^+)$ predictions have

errors below 10% and $y(\text{H}_2^+)$ is typically below 10^{-10} , this deviation is unlikely to affect the overall evolution.

Temperature is a key variable for star formation because it directly affects the gas pressure and hence the gas dynamics. Our DeepONet-based emulator reproduces the temperature with very high accuracy: in more than 99% (97%) of the test cases, the temperature error is below 10% (5%), demonstrating the effectiveness of the emulator.

3.1.2. Emulating thermal and chemical evolution in a one-zone calculation

To test whether our DeepONet-based emulator can reproduce the thermochemical evolution in Pop III star formation, we perform a one-zone collapse calculation using predictions from the emulator. In this section, we adopt a timestep of $\Delta t = 0.1 t_{\text{ff}}$ and update the state with simple iterative predictions, without the timescale-based modification described in Section 2.3.

Figure 4 shows the results of the one-zone calculations. The upper and lower panels show the temperature and chemical evolution, respectively. For $n_{\text{H}} \leq 10^{18} \text{ cm}^{-3}$, the solid lines show the ground-truth results obtained by numerically integrating Eqs. (1) and (2), while the dashed lines show the results of DeepONet predictions. For $n_{\text{H}} \geq 10^{18} \text{ cm}^{-3}$, where the chemical equilibrium is a good approximation, the solid lines show the ground-truth results obtained by numerically integrating Eq. (2) with abundances given by the Saha equation, while the dashed lines show adiabatic evolution along a sequence of chemical equilibrium states obtained by interpolating a precomputed table (see Appendix B).

As shown in Figure 4, the DeepONet-based emulator accurately reproduces the reference evolution for $n_{\text{H}} \leq 10^{18} \text{ cm}^{-3}$, where nonequilibrium chemistry and radiative cooling are essential. In addition, the table-interpolation method also reproduces the reference evolution well in the high-density equilibrium and adiabatic regime until the gas reaches the protostellar density of $n_{\text{H}} \sim 10^{22} \text{ cm}^{-3}$.

These results demonstrate that our emulator can follow the thermochemical evolution for $4.5 \times 10^{-3} \text{ cm}^{-3} \leq n_{\text{H}} \leq 10^{18} \text{ cm}^{-3}$ and, when combined with the table-interpolation method, across the entire density range relevant to Pop III star formation ($4.5 \times 10^{-3} \text{ cm}^{-3} \leq n_{\text{H}} \leq 10^{22} \text{ cm}^{-3}$). To the best of our knowledge, this is the first study to successfully emulate thermochemical evolution using NNs across such a wide density range.

It should be noted, however, that simple DeepONet predictions can reproduce the reference evolution only when the timestep is relatively long (e.g., $\Delta t = 0.1 t_{\text{ff}}$). As shown in Section 3.2.3, simply iterating the predictions with short timesteps leads to deviations from

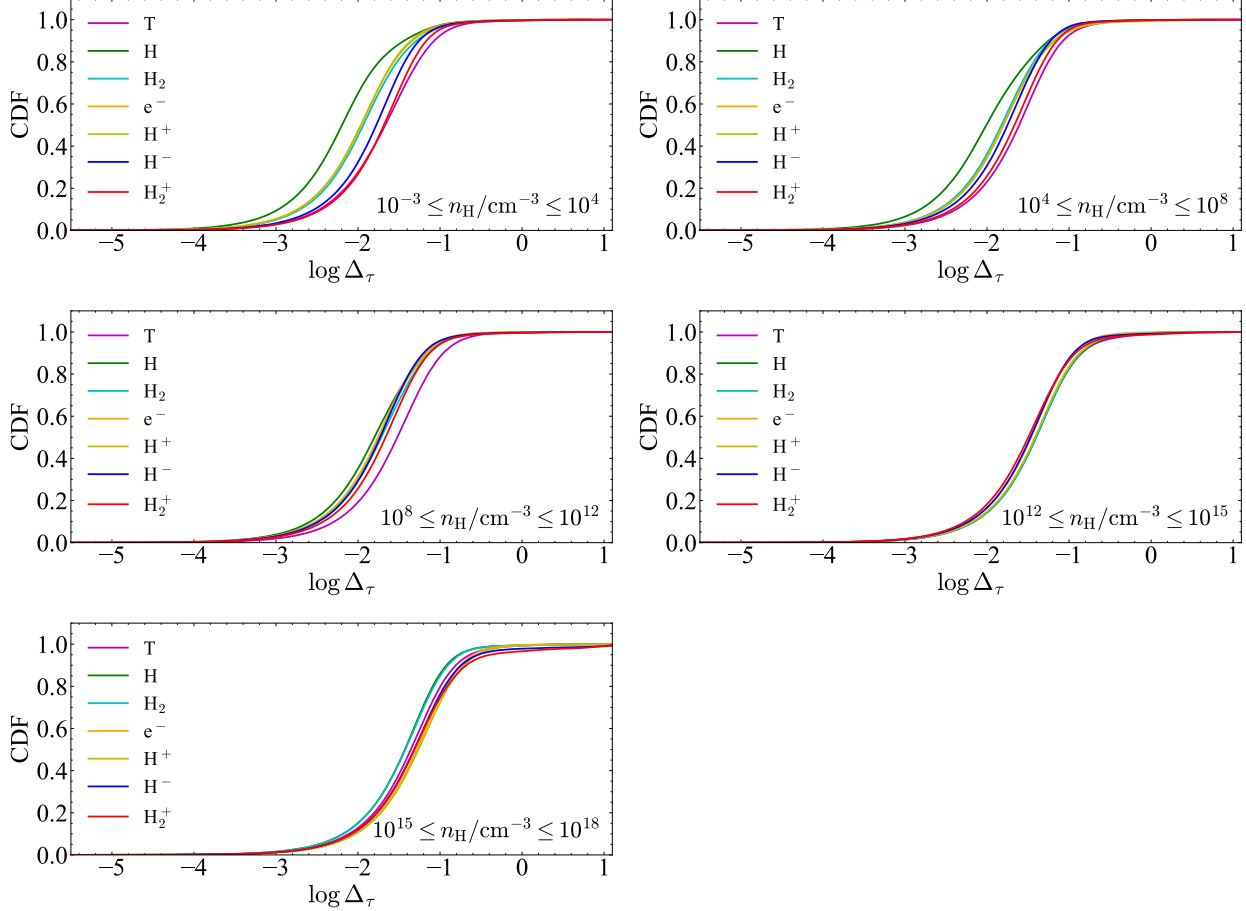


Figure 5. Same as Figure 3, but for the characteristic timescales τ_ϵ with $\epsilon = 0.1$. The horizontal axis shows the logarithm of Δ_τ as defined in Eq. (20).

the reference evolution, thereby requiring the timescale-based method.

3.2. Iterative Predictions with Short Timesteps

Next, we address the issue of unphysical evolution caused by iterative predictions with short timesteps. We will see that this problem can be mitigated by our timescale-based method (Section 2.3).

In Section 3.2.1, we evaluate the performance of the DGM-based timescale estimator used in our timescale-based method. We then demonstrate the effectiveness of our method in two test cases: evolution from a fixed-density initial state (Section 3.2.2) and one-zone collapse calculations (Section 3.2.3). In both cases, simple iteration of DeepONet predictions fails to reproduce the true evolution, but our timescale-based method yields robust predictions even under short iterative timesteps.

3.2.1. Estimating characteristic timescales

In addition to the DeepONet-based NNs for predictions of thermochemical evolution, we construct DGM-

based NNs to estimate the timescale τ_ϵ , that is, the interval over which physical evolution changes a target variable by a fraction ϵ . This timescale is used in the timescale-based method given by Eq. (8). As mentioned in Section 2.3, we adopt $\epsilon = 0.1$ when obtaining τ_ϵ , because typical errors of the DeepONet predictions are significantly smaller than 10% for all variables except for H_2^+ , whose abundance is very small and hardly affects the overall evolution (Figure 3; Table 2).

To assess the accuracy of the DGM estimator of τ_ϵ , we construct a test data set of 5.12×10^5 samples that is independent of the training and validation sets and examine the resulting error distribution. The estimation error is defined as

$$\Delta_\tau = |Y_{\tau,\text{pred}} - Y_{\tau,\text{true}}|, \quad (20)$$

where Y_τ is a function of τ_ϵ introduced in Eq. (16), and the subscripts “true” and “pred” refer to the numerically computed ground-truth value and the NN estimate, respectively. As described in Section 2.3, the network is trained to minimize a loss function based on Y_τ .

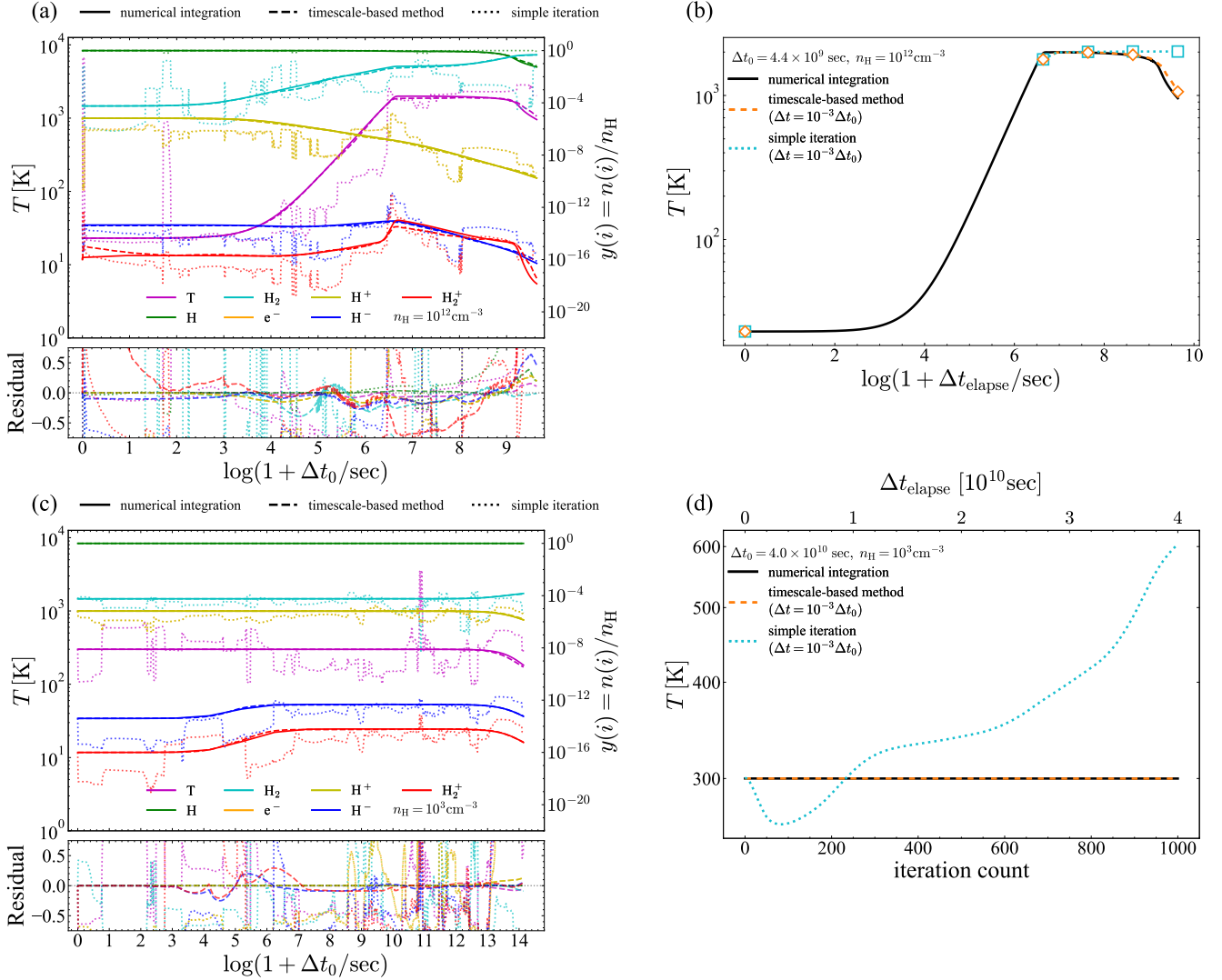


Figure 6. Comparison of fixed-density evolution using simple iteration of DeepONet predictions (dotted), the timescale-based method (dashed), and numerical integration (solid). (a) Same as Figure 2 but for iterative updates. The horizontal axis is the overall timestep Δt_0 , which is divided into 1000 equal substeps of $\Delta t = \Delta t_0/1000$ for iterations. (b) Step-by-step temperature evolution for the case of $\Delta t_0 = \Delta t_{\text{max}} = 4.4 \times 10^9 \text{sec}$ in panel (a). (c) Same as panel (a) but for the case with the initial temperature $T = 300 \text{K}$ and fixed density $n_H = 10^3 \text{cm}^{-3}$. (d) Step-by-step temperature evolution for the case of $\Delta t_0 = 4.0 \times 10^{10} \text{sec}$ in panel (c). In panels (a) and (c), colors are the same as in Figure 2, and $y(e^-)$ and $y(H^+)$ nearly coincide. The bottom panels of (a) and (c) show the residual errors, with line styles corresponding to those in the panels above. In panel (b), the horizontal axis shows the elapsed time $\Delta t_{\text{elapse}} = i \Delta t$ at the iteration count i , with markers indicating the initial state and the 1st, 10th, 100th, and 1000th iterations. In panel (d), the bottom horizontal axis shows the iteration count, while the top axis indicates Δt_{elapse} .

Figure 5 shows the CDF of $\Delta \tau$ for each target variable in each density region (Section 2.3). Most of the errors are below $\Delta \tau = 10^{-1}$; the only exception is temperature in Region 4, yet the errors are still concentrated below $10^{-0.5}$. The DGM-based NN estimates the characteristic timescales with reasonable accuracy.

This level of accuracy is sufficient for the timescale-based method to ensure robust iterative predictions. By

construction, our method is not sensitive to the exact value of τ_ϵ , because the update formula (Eq. (8)) incorporates τ_ϵ only indirectly. We will confirm that our timescale-based method with the DGM timescale estimator successfully models the thermochemical evolution in the following sections.

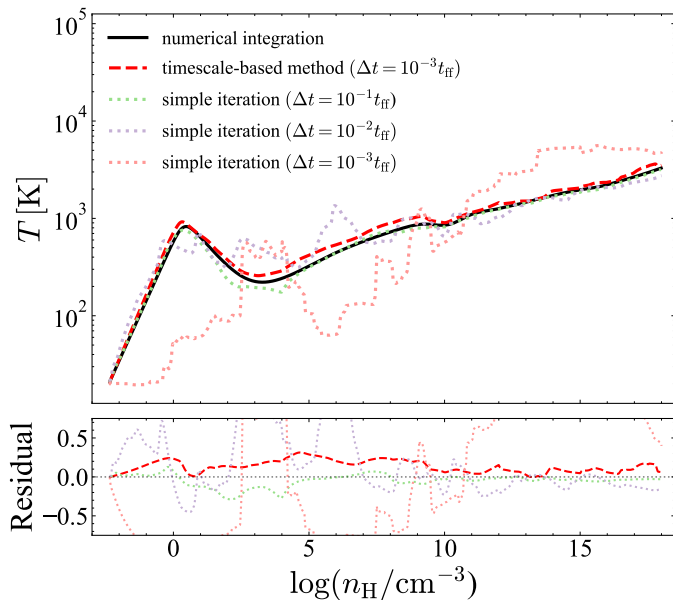


Figure 7. Same as the top and bottom panels of Figure 4, but with different time steps: $\Delta t = 10^{-1}$ (green), 10^{-2} (purple), and $10^{-3} t_{\text{ff}}$ (red). We show the evolution using simple iteration of DeepONet predictions (dotted), the timescale-based method (dashed), and numerical integration (solid). Although only the case with $\Delta t = 10^{-3} t_{\text{ff}}$ is shown for the timescale-based method, the results for different timesteps, such as 10^{-1} , 10^{-2} , and $10^{-4} t_{\text{ff}}$, are approximately the same.

3.2.2. Short-timestep iterative predictions at fixed density

In this section, we study iterative updates of the thermochemical states at fixed density, starting from a given initial condition. We show that simply iterating DeepONet predictions can lead to unphysical evolution either through error accumulation (P. van de Bor et al. 2025) or through missed long-term transitions. We also show that this issue is resolved by the timescale-based method introduced in Section 2.3.

To begin with, we employ the same setup as in Section 3.1.1 but update the state with short iterative time steps. We define 1000 outer steps, $\log(1 + \Delta t_0/\text{sec}) = (i/1000) \log(1 + \Delta t_{\text{max}}/\text{sec})$ ($i = 1, \dots, 1000$), and divide each into 1000 equal substeps, $\Delta t = \Delta t_0^{(i)}/1000$. At each substep, we update the temperature and chemical abundances using two emulators: one simply updates the state with the DeepONet predictions, and the other uses the update formula of the timescale-based method (Eq. (8)).

Figure 6(a) shows the thermochemical evolution obtained by iteratively applying the two emulators. Here, we use the same initial conditions as in Figure 2. Dashed and dotted lines show the results from simple DeepONet iterations and from the timescale-based method,

respectively. Although the single-step DeepONet predictions accurately reproduce the reference evolution (Figure 2), simply repeating the DeepONet updates with short timesteps causes large deviations. The results from the timescale-based method, however, remain accurate even under repeated application.

The emulator using simple DeepONet predictions does not enforce hydrogen–nucleus conservation or charge neutrality at each substep, but we have confirmed that adding these constraints does not improve the results. Note that the timescale-based method applies both conservation laws at every substep (Section 2.3).

To identify the origin of these deviations, we examine the step-by-step evolution. Figure 6(b) shows the step-by-step temperature evolution in a case with $\Delta t_0 = \Delta t_{\text{max}} = 4.4 \times 10^9$ sec, where simple DeepONet iterations miss long-term transitions. The horizontal axis shows the cumulative elapsed time, $\Delta t_{\text{elapse}} = i \Delta t$ ($i = 0, 1, \dots, 1000$), corresponding to the iteration count. The solid black line shows the ground-truth numerical integration; the orange dashed line with markers shows the timescale-based method; and the light-blue dotted line with markers shows simple DeepONet iterations. The markers indicate the initial state and the 1st, 10th, 100th, and 1000th iterations.

At the first substep ($\Delta t = 4.4 \times 10^6$ sec), both emulators raise the temperature to the correct plateau value, $T \simeq 2 \times 10^3$ K, because the physical change is large ($\Delta t > \tau_e$) and the timescale-based method yields the simple DeepONet value. They remain on this plateau until $\Delta t \approx 10^9$ sec. At later times, simply iterating the DeepONet updates misses the slow H_2 cooling and overestimates the temperature, because the relatively small physical change at each substep is masked by larger prediction errors. In contrast, the timescale-based method continues to follow the reference evolution.

Next, we examine a case in which the accumulation of prediction errors is evident. Figure 6(c) is similar to panel (a) but assumes a fixed density of $n_{\text{H}} = 10^3 \text{ cm}^{-3}$ and an initial temperature of $T = 300$ K. In this setup, the reference evolution remains nearly constant for all variables, which makes this setup well suited for investigating error accumulation under simple iterations. The simple iterative updates fail to keep the variables nearly constant, whereas the timescale-based method reproduces the nearly constant reference evolution with only gradual changes.

Figure 6(d) shows the step-by-step temperature evolution for the case in panel (c) with $\Delta t_0 = 4.0 \times 10^{10}$ sec. The figure is similar to panel (b), but the bottom axis denotes the iteration count, with the top axis showing the corresponding elapsed time Δt_{elapse} . This choice of

axes makes the random-walk behavior of the simple iterative updates clearer.

The simple iterations fail to maintain a constant temperature: the temperature first drops and then rises in a random-walk manner, as expected when the accumulation of prediction errors dominates the evolution. The final temperature reaches 600 K, twice the constant reference value of 300 K. In contrast, the timescale-based method accurately reproduces the constant evolution.

To summarize, our timescale-based method both suppresses the accumulation of prediction errors and preserves long-term evolution, even under iterative updates with short timesteps. These results suggest that our timescale-based emulator can robustly predict the thermochemical evolution under many short timesteps. In the next section, we verify this capability in one-zone collapse calculations.

3.2.3. One-zone calculations with short-timestep iterative predictions

In this section, we evaluate the timescale-based method in one-zone collapse calculations. While Section 3.1.2 used a relatively large time step, $\Delta t = 0.1 t_{\text{ff}}$, we adopt much smaller time steps of $\Delta t = 10^{-2}$, 10^{-3} , and $10^{-4} t_{\text{ff}}$ to mimic the short timesteps that can occur in hydrodynamic simulations. We compare results from the simple DeepONet emulator and the timescale-based method, focusing on issues that emerge at short timesteps.

Figure 7 shows the temperature evolution in one-zone calculations with different timesteps. Dotted and dashed lines show the results from the simple DeepONet emulator and the timescale-based method, respectively. The solid line shows the ground-truth numerical integration result.

The simple DeepONet updates deviate increasingly from the reference evolution as Δt decreases, with significant departures seen when $\Delta t \lesssim 10^{-2} t_{\text{ff}}$. We omit the case with $\Delta t = 10^{-4} t_{\text{ff}}$ in the figure, as the deviation is already significant at $\Delta t = 10^{-3} t_{\text{ff}}$.

The results from the timescale-based method agree well with the reference evolution even for $\Delta t \leq 10^{-2} t_{\text{ff}}$. We show only the $10^{-3} t_{\text{ff}}$ case, since the results for $\Delta t = 10^{-1}$, 10^{-2} , and $10^{-4} t_{\text{ff}}$ are approximately the same.

These results confirm that our timescale-based method can emulate the thermochemical evolution in Pop III star formation accurately and robustly even under extremely small timesteps. Our approach is therefore suited for future incorporation into hydrodynamic simulations.

4. DISCUSSION

4.1. Computational Time

To assess the speed-up provided by the NN models, we measure their computational time on an AMD EPYC 7643 CPU and an NVIDIA A6000 GPU. Section 4.1.1 examines the cost of single-step predictions, and Section 4.1.2 discusses the computational cost when the emulator is applied to one-zone collapse calculations.

4.1.1. Single-step predictions

First, we measure the computational times for single-step DeepONet predictions and for conventional numerical integration. Both methods are tested on the same set of 5.12×10^5 random initial conditions, with a timestep of $\Delta t = \Delta t_{\text{max}}$. Numerical integration is performed under the constraint that the relative change of any variable (temperature or any chemical abundance) at each substep does not exceed 10% (see also Section 2.4).

Table 3 summarizes the mean and standard deviation of the CPU computational times for numerical integration and DeepONet prediction in each density region. Roughly speaking, DeepONet prediction is about 10 times faster than numerical integration. Numerical integration in Region 0 takes longer than in the other regions, since $\Delta t = \Delta t_{\text{max}} = 10^{0.5} t_{\text{ff}} \propto n_{\text{H}}^{-0.5}$ (Section 2.4) is larger and thus requires more substeps to satisfy the 10% relative-change constraint. Note that these time measurements are for simple DeepONet predictions. For the timescale-based method, the cost increases by about 50%, due to the extra cost of the DGM model for estimating τ_{ϵ} .

DeepONet prediction also reduces the standard deviation of computational times by more than two orders of magnitude. The large spread observed in numerical integration is due to its sensitivity to the initial state: samples far from equilibrium require many substeps for numerical integration. Such variability limits parallel efficiency because faster cells must wait for slower ones.

In addition, we measure the GPU computational times for DeepONet prediction, combining all 5.12×10^5 input samples into a single batch processed at once. On the GPU, DeepONet prediction is more than three (two) orders of magnitude faster than numerical integration (DeepONet predictions on the CPU). In the measurement, we use an NVIDIA RTX A6000 with 10,752 CUDA cores. We also test smaller batch sizes and find that the computational time does not change significantly until the batch size becomes smaller than 5,000, suggesting that the GPU becomes saturated around a batch size of $\sim 5,000$.

These results suggest that NN emulators, such as our DeepONet model, are well suited to large-scale parallel

Table 3. Summary of computational time for single-step updates in each region.

	Region 0	Region 1	Region 2	Region 3	Region 4
Mean [CPUms] (NI)	21	6.6	2.7	3.9	3.6
Mean [CPUms] (NN)	0.53	0.65	0.75	0.74	0.74
Mean speedup [\times] (NN vs NI)	40	10	3.7	5.2	4.9
Standard deviation [CPUms] (NI)	60	11	1.6	1.6	1.4
Standard deviation [CPUms] (NN)	0.11	0.12	0.071	0.065	0.059

NOTE— Top and second rows: mean computational time for single-step updates for numerical integration (NI) and the DeepONet-based NN predictions (NN), respectively. Third row: speed-up of mean computational time for NN compared with NI. Fourth and fifth rows: standard deviation in the computational time for NI and NN. See the note of Table 2 for the definition of each density region.

simulations owing to their low variance in computational times. Furthermore, such emulators have the potential to enable even faster modeling of thermochemical evolution in GPU-accelerated simulations.

4.1.2. One-zone calculations

Next, we measure the computational times of one-zone calculations with $\Delta t = 0.1 t_{\text{ff}}$ for the emulator using the timescale-based method and for conventional numerical integration. We replicate the same initial state into a batch of 32^3 cells to mimic a workload in three-dimensional simulations. We measure the emulator computational time on both the CPU and the GPU. The GPU processes the entire batch in a single call, as described in Section 4.1.1.

On the CPU, the emulator is slightly slower than numerical integration because numerical integration requires fewer substeps under near-equilibrium one-zone conditions than for random initial conditions. In full three-dimensional simulations, however, shocks and other dynamical processes likely drive the gas far from equilibrium and increase the integration cost. Under those conditions, we expect the emulator, which is insensitive to initial conditions, to outperform numerical integration (see Section 4.1.1).

The GPU greatly accelerates the emulator: GPU emulation is roughly 35 times faster than numerical integration. Given the growing availability of GPUs and the recent development of GPU-supported hydrodynamic codes, such as CHOLLA (E. E. Schneider & B. E. Robertson 2015), GAMER-2 (H.-Y. Schive et al. 2018), QUOKKA (B. D. Wibking & M. R. Krumholz 2022), and AthenaK (J. M. Stone et al. 2024), we expect that NN-based emulators for thermochemical evolution, including ours, will provide substantial benefits for future hydrodynamic simulations.

4.2. Comparison with Previous Work

We first compare our results with L. Branca & A. Pallottini (2024), who used DeepONet to model the low-density ISM ($n_{\text{H}} \lesssim 10^4 \text{ cm}^{-3}$) under an external radiation field. In contrast, we have considered a much broader density range, $10^{-3} \text{ cm}^{-3} \leq n_{\text{H}} \leq 10^{18} \text{ cm}^{-3}$, relevant to Pop III star formation, and followed the evolution without radiation. Moreover, whereas L. Branca & A. Pallottini (2024) trained their NNs for short timesteps of Δt from 0 to 1 kyr using a linear time scale, we trained ours for the much wider timesteps of Δt from 0 sec to $10^{0.5} t_{\text{ff}}$ (which is $\gtrsim 1 \text{ Myr}$ at $n_{\text{H}} \lesssim 10^4 \text{ cm}^{-3}$) using a logarithmic time scaling, as in L. Branca & A. Pallottini (2023).

We obtained overall accuracies comparable to those of L. Branca & A. Pallottini (2024), except for H^- and H_2^+ , whose errors are about an order of magnitude larger than those reported in the literature. This reduced accuracy is not critical, since these species are often rare and have a negligible impact on the global evolution. The validity of our NN-based emulators has been demonstrated by their successful application to one-zone calculations (Sections 3.1.2 and 3.2.3).

Next, we discuss the issue of simple iterative NN updates leading to unphysical evolution, in part due to the accumulation of prediction errors (P. van de Bor et al. 2025). For iterative updates at fixed density, we confirmed this behavior and showed that such updates can also fail to capture long-term changes (Section 3.2.2). Similarly, we found that simple iterative NN updates lead to significant deviations from the reference thermal trajectory in one-zone calculations with short timesteps (Section 3.2.3).

The timescale-based method introduced in Section 2.3 resolves these issues (Sections 3.2.2 and 3.2.3). This method enables robust iterative predictions even under

short-timestep updates, as typically required in hydrodynamic simulations.

Our timescale-based method differs from previous approaches proposed to mitigate issues arising from iterative NN updates in autoencoder-based models, such as injecting Gaussian noise during training (J. Holdship et al. 2021) and training the iterative updates themselves (S. Maes et al. 2024). These methods are known to increase one-step prediction errors (J. Holdship et al. 2021; S. Maes et al. 2024). In contrast, our method keeps one-step prediction errors low because the original NN prediction is used when the predicted change exceeds the estimated prediction error.

5. CONCLUSION

In this study, we developed a neural-network (NN) emulator that models the thermal and chemical evolution of Pop III star formation over the wide density range $10^{-3} \text{ cm}^{-3} \leq n_{\text{H}} \leq 10^{18} \text{ cm}^{-3}$. To make accurate predictions over such a wide range, we divided the range into five subregions and trained separate DeepONet models for each region.

Furthermore, to ensure robust predictions even when many short-timestep iterations are required, we introduced a new update method based on the timescale for significant variation. Specifically, we constructed DGM-based NNs to estimate the timescale τ_{ϵ} defined as the minimum time over which a physical change significantly exceeds the typical errors of DeepONet predictions. If the given timestep Δt is shorter than τ_{ϵ} , the change over Δt is computed by scaling the DeepONet change over τ_{ϵ} by $\Delta t/\tau_{\epsilon}$.

We demonstrated that our emulator accurately reproduces the thermochemical evolution. It performs well both for fixed-density evolution and for one-zone calculations that mimic typical star-formation conditions. For 5.12×10^5 random states, the emulator matches gas temperature and the abundances to $< 10\%$ relative er-

ror in $\gtrsim 90\%$ of cases, except for slightly larger scatter for H_2^+ . Even when the timestep is greatly reduced and many iterations are needed, the newly developed timescale-based method robustly reproduces the thermochemical evolution. In terms of performance, our tests indicated that the emulator is about ten times faster than conventional numerical integration on the CPU, and more than a thousand times faster in batched GPU calculations.

NN emulators of thermochemical evolution are well suited for integration into three-dimensional star-formation simulations. The computational speedup and the better parallel efficiency are particularly advantageous for large-scale parallel or GPU-accelerated calculations. Although our current models target a metal-free and radiation-free gas, we plan to incorporate additional physics, such as metals and radiative feedback, to broaden the applicability. We also plan to integrate our emulator into hydrodynamic simulations of Pop III star formation, opening a new path to exploring star formation using simulations accelerated by chemical emulators.

ACKNOWLEDGMENTS

The authors thank Hajime Fukushima, Kazutaka Kimura, Kazuyuki Omukai, Keiichi Maeda, Takashi Hosokawa, and Takashi Okamoto for fruitful discussions and comments. The numerical calculations were performed on the GPU system and HPE Cray XD2000 at the Center for Computational Astrophysics at the National Astronomical Observatory of Japan. This work was supported by JSPS KAKENHI Grant Numbers 24H00002 (KS). This research was also supported by MEXT as ‘‘Program for Promoting Researches on the Supercomputer Fugaku’’ (Structure and Evolution of the Universe Unraveled by Fusion of Simulation and AI, JPMXP1020230406).

APPENDIX

A. CHEMICAL REACTIONS

In this study, we considered a total of 18 chemical reactions relevant to primordial gas chemistry. These include key collisional and associative processes that govern the formation and destruction of molecular hydrogen and other species in metal-free environments. The full list of reactions is provided in Table 4.

B. TABLE-INTERPOLATION METHOD FOR HIGH-DENSITY EQUILIBRIUM AND ADIABATIC REGIME

For $n_{\text{H}} \geq 10^{18} \text{ cm}^{-3}$, reaction timescales are so short that the chemical evolution proceeds along a sequence of chemical equilibrium states set by density and temperature according to the Saha equation (M. N. Saha 1920). Moreover, at such high densities, radiative cooling via line and continuum emission is so inefficient that the specific

entropy is approximately conserved and the gas can be treated as adiabatic (K. Omukai 2001). In the operator-splitting approach, the total energy, consisting of internal and chemical energy, does not change during the stage of chemical and thermal updates given by Eqs. (1) and (2).

Therefore, in this high-density equilibrium and adiabatic regime, the updated chemical abundances $y(i)$ and the temperature T can be uniquely determined from the pair of variables n_{H} and the total energy per hydrogen atom E_{tot} . Here, E_{tot} is given by

$$E_{\text{tot}} = U + E_{\text{chem}}, \quad (\text{B1})$$

where U and E_{chem} are the internal energy and chemical energy per hydrogen atom, respectively. We calculate the internal energy U as

$$U = \frac{3}{2}k_{\text{B}}T \left(\sum_{i=1}^6 y(i) + y_{\text{He}} \right) + \left(\int_{0\text{K}}^T c_{v,\text{H}_2}(T') dT' - \frac{3}{2}k_{\text{B}}T \right) y(\text{H}_2), \quad (\text{B2})$$

with the temperature-dependent heat capacity of molecular hydrogen $c_{v,\text{H}_2}(T)$ (K. Sugimura et al. 2023; see D. C. Black & P. Bodenheimer 1975 for the calculation method), which accounts for rovibrational excitations. The chemical energy E_{chem} is given by

$$E_{\text{chem}} = \sum_{i=1}^6 y(i) \chi(i), \quad (\text{B3})$$

where $\chi(i)$ is the chemical energy of species i measured with respect to H_2 . We set $\chi(\text{H}) = 216.034$, $\chi(\text{H}_2) = 0$, $\chi(\text{e}^-) = 0$, $\chi(\text{H}^+) = 1528.084$, $\chi(\text{H}^-) = 143.246$, and $\chi(\text{H}_2^+) = 1488.365$ (in kJ mol^{-1}), from the KIDA database (V. Wakelam et al. 2012).

Given that the updated $y(i)$ and T are determined by n_{H} and E_{tot} , the chemical and thermal updates obtained by numerically integrating Eqs. (1) and (2) can be replaced by interpolating a precomputed two-dimensional table on a grid in $(n_{\text{H}}, E_{\text{tot}})$ space. Because the table is two-dimensional, the table size needed for accurate interpolation is reasonably small. Therefore, we adopt the table-interpolation method rather than NN-based emulators in this high-density regime. Like NN-based emulators, the table-interpolation method yields a small standard deviation of computational time and enables efficient batch processing, making it well suited to large-scale parallel and GPU-accelerated simulations.

In our implementation, we tabulate n_{H} from 10^{18} to 10^{22} cm^{-3} on a 1000-point logarithmic grid. We also tabulate E_{tot} on a 1000-point logarithmic grid over the range corresponding to $10\text{K} < T < 10^5\text{K}$, which covers the values relevant for Pop III star formation. To construct the table, for each grid point $(n_{\text{H}}, E_{\text{tot}})$, we obtain the combination of $y(i)$ and T that satisfies the Saha equation with the total energy equal to the given E_{tot} . To compute the updated $y(i)$ and T , we perform linear interpolation of this table in logarithmic space. We demonstrate the accuracy of this table-interpolation method by applying it to a one-zone collapse calculation in Section 3.1.2.

REFERENCES

- Abadi, M., Agarwal, A., Barham, P., et al. 2015, TensorFlow: Large-Scale Machine Learning on Heterogeneous Systems, <https://www.tensorflow.org/>
- Abel, T., Anninos, P., Zhang, Y., & Norman, M. L. 1997, NewA, 2, 181, doi: [10.1016/S1384-1076\(97\)00010-9](https://doi.org/10.1016/S1384-1076(97)00010-9)
- Abel, T., Bryan, G. L., & Norman, M. L. 2002, Science, 295, 93, doi: [10.1126/science.1063991](https://doi.org/10.1126/science.1063991)
- Black, D. C., & Bodenheimer, P. 1975, ApJ, 199, 619, doi: [10.1086/153729](https://doi.org/10.1086/153729)
- Branca, L., & Pallottini, A. 2023, MNRAS, 518, 5718, doi: [10.1093/mnras/stac3512](https://doi.org/10.1093/mnras/stac3512)
- Branca, L., & Pallottini, A. 2024, A&A, 684, A203, doi: [10.1051/0004-6361/202449193](https://doi.org/10.1051/0004-6361/202449193)
- Bromm, V., Coppi, P. S., & Larson, R. B. 2002, ApJ, 564, 23, doi: [10.1086/323947](https://doi.org/10.1086/323947)
- de Mijolla, D., Viti, S., Holdship, J., Manolopoulou, I., & Yates, J. 2019, A&A, 630, A117, doi: [10.1051/0004-6361/201935973](https://doi.org/10.1051/0004-6361/201935973)
- Forrey, R. C. 2013, ApJL, 773, L25, doi: [10.1088/2041-8205/773/2/L25](https://doi.org/10.1088/2041-8205/773/2/L25)
- Fukushima, H., Omukai, K., & Hosokawa, T. 2018, MNRAS, 473, 4754, doi: [10.1093/mnras/stx2620](https://doi.org/10.1093/mnras/stx2620)
- Galli, D., & Palla, F. 1998, A&A, 335, 403

Table 4. Chemical reactions considered in this study

Index	Reactions	References	Index	Reactions	References
1	$\text{H} + \text{e}^- \rightarrow \text{H}^+ + 2\text{e}^-$	[1]	10	$\text{H} + \text{e}^- \rightarrow \text{H}^- + \gamma$	[4]
2	$\text{H}^+ + \text{e}^- \rightarrow \text{H} + \gamma$	[2]	11	$2\text{H} \rightarrow \text{H}^+ + \text{e}^- + \text{H}$	[7]
3	$\text{H}^- + \text{H} \rightarrow \text{H}_2 + \text{e}^-$	[3]	12	$\text{H}^- + \text{e}^- \rightarrow \text{H} + 2\text{e}^-$	[1]
4	$\text{H}_2 + \text{H}^+ \rightarrow \text{H}_2^+ + \text{H}$	[4]	13	$\text{H}^- + \text{H}^+ \rightarrow \text{H}_2^+ + \text{e}^-$	[4]
5	$\text{H}_2 + \text{e}^- \rightarrow 2\text{H} + \text{e}^-$	[4]	14	$\text{H}^- + \text{H}^+ \rightarrow 2\text{H}$	[4]
6	$\text{H}_2 + \text{H} \rightarrow 3\text{H}$	[5]	15	$\text{H} + \text{H}^+ \rightarrow \text{H}_2^+ + \gamma$	[4]
7	$3\text{H} \rightarrow \text{H}_2 + \text{H}$	[6]	16	$\text{H}_2^+ + \text{H} \rightarrow \text{H}_2 + \text{H}^+$	[4]
8	$2\text{H} + \text{H}_2 \rightarrow 2\text{H}_2$	[7]	17	$\text{H}_2^+ + \text{e}^- \rightarrow 2\text{H}$	[4]
9	$2\text{H}_2 \rightarrow 2\text{H} + \text{H}_2$	[7,8]	18	$\text{H}_2^+ + \text{H}^- \rightarrow \text{H}_2 + \text{H}$	[9]

References—[1] T. Abel et al. (1997), [2] S. C. O. Glover & A.-K. Jappsen (2007), [3] H. Kreckel et al. (2010), [4] D. Galli & F. Palla (1998), [5] P. G. Martin et al. (1996), [6] R. C. Forrey (2013), [7] F. Palla et al. (1983), [8] P. R. Shapiro & H. Kang (1987), [9] T. Millar et al. (1991)

- Glorot, X., Bordes, A., & Bengio, Y. 2011, in Proceedings of the fourteenth international conference on artificial intelligence and statistics, JMLR Workshop and Conference Proceedings, 315–323
- Glover, S. C. O. 2015, MNRAS, 451, 2082, doi: [10.1093/mnras/stv1059](https://doi.org/10.1093/mnras/stv1059)
- Glover, S. C. O., & Jappsen, A.-K. 2007, The Astrophysical Journal, 666, 1, doi: [10.1086/519445](https://doi.org/10.1086/519445)
- Grassi, T., Merlin, E., Piovan, L., Buonomo, U., & Chiosi, C. 2011, arXiv e-prints, arXiv:1103.0509, doi: [10.48550/arXiv.1103.0509](https://doi.org/10.48550/arXiv.1103.0509)
- Grassi, T., Nauman, F., Ramsey, J. P., et al. 2022, A&A, 668, A139, doi: [10.1051/0004-6361/202039956](https://doi.org/10.1051/0004-6361/202039956)
- Grichener, A., Renzo, M., Kerzendorf, W. E., et al. 2025, ApJS, 279, 49, doi: [10.3847/1538-4365/ade717](https://doi.org/10.3847/1538-4365/ade717)
- Heyl, J., Viti, S., & Vermariën, G. 2023, Faraday Discussions, 245, 569, doi: [10.1039/D3FD00008G](https://doi.org/10.1039/D3FD00008G)
- Hoerl, A. E., & Kennard, R. W. 1970a, Technometrics, 12, 55
- Hoerl, A. E., & Kennard, R. W. 1970b, Technometrics, 12, 69
- Holdship, J., Viti, S., Haworth, T. J., & Ilee, J. D. 2021, A&A, 653, A76, doi: [10.1051/0004-6361/202140357](https://doi.org/10.1051/0004-6361/202140357)
- Hosokawa, T., Omukai, K., Yoshida, N., & Yorke, H. W. 2011, Science, 334, 1250, doi: [10.1126/science.1207433](https://doi.org/10.1126/science.1207433)
- Kingma, D. P., & Ba, J. 2014, arXiv e-prints, arXiv:1412.6980, doi: [10.48550/arXiv.1412.6980](https://doi.org/10.48550/arXiv.1412.6980)
- Klessen, R. S., & Glover, S. C. O. 2023, ARA&A, 61, 65, doi: [10.1146/annurev-astro-071221-053453](https://doi.org/10.1146/annurev-astro-071221-053453)
- Kreckel, H., Bruhns, H., Čížek, M., et al. 2010, Science, 329, 69, doi: [10.1126/science.1187191](https://doi.org/10.1126/science.1187191)
- Lu, L., Jin, P., Pang, G., Zhang, Z., & Karniadakis, G. E. 2021a, NatMI, 3, 218, doi: [10.1038/s42256-021-00302-5](https://doi.org/10.1038/s42256-021-00302-5)
- Lu, L., Meng, X., Mao, Z., & Karniadakis, G. E. 2021b, SIAMR, 63, 208, doi: [10.1137/19M1274067](https://doi.org/10.1137/19M1274067)
- Maes, S., De Ceuster, F., Van de Sande, M., & Decin, L. 2024, ApJ, 969, 79, doi: [10.3847/1538-4357/ad47a1](https://doi.org/10.3847/1538-4357/ad47a1)
- Martin, P. G., Schwarz, D. H., & Mandy, M. E. 1996, ApJ, 461, 265, doi: [10.1086/177053](https://doi.org/10.1086/177053)
- Matsukoba, R., Takahashi, S. Z., Sugimura, K., & Omukai, K. 2019, MNRAS, 484, 2605, doi: [10.1093/mnras/sty3522](https://doi.org/10.1093/mnras/sty3522)
- Millar, T., Bennett, A., Rawlings, J., Brown, P., & Charnley, S. 1991, A&AS, 87, 585
- Nagakura, T., & Omukai, K. 2005, MNRAS, 364, 1378, doi: [10.1111/j.1365-2966.2005.09685.x](https://doi.org/10.1111/j.1365-2966.2005.09685.x)
- Nakauchi, D., Omukai, K., & Susa, H. 2019, MNRAS, 488, 1846, doi: [10.1093/mnras/stz1799](https://doi.org/10.1093/mnras/stz1799)
- Navarro, L. M., Martin-Moreno, L., & Rodrigo, S. G. 2023, EJPh, 45, 015803, doi: [10.1088/1361-6404/ad0a9f](https://doi.org/10.1088/1361-6404/ad0a9f)
- Omukai, K. 2001, ApJ, 546, 635, doi: [10.1086/318296](https://doi.org/10.1086/318296)
- Omukai, K., & Nishi, R. 1998, ApJ, 508, 141, doi: [10.1086/306395](https://doi.org/10.1086/306395)
- Palla, F., Salpeter, E. E., & Stahler, S. W. 1983, ApJ, 271, 632, doi: [10.1086/161231](https://doi.org/10.1086/161231)
- Palud, P., Einig, L., Le Petit, F., et al. 2023, A&A, 678, A198, doi: [10.1051/0004-6361/202347074](https://doi.org/10.1051/0004-6361/202347074)
- Paszke, A., Gross, S., Massa, F., et al. 2019, arXiv e-prints, arXiv:1912.01703, doi: [10.48550/arXiv.1912.01703](https://doi.org/10.48550/arXiv.1912.01703)
- Raissi, M., Perdikaris, P., & Karniadakis, G. 2019, JCoPh, 378, 686, doi: [10.1016/j.jcp.2018.10.045](https://doi.org/10.1016/j.jcp.2018.10.045)
- Sadanari, K. E., Omukai, K., Sugimura, K., Matsumoto, T., & Tomida, K. 2021, MNRAS, 505, 4197, doi: [10.1093/mnras/stab1330](https://doi.org/10.1093/mnras/stab1330)

- Sadanari, K. E., Omukai, K., Sugimura, K., Matsumoto, T., & Tomida, K. 2023, MNRAS, 519, 3076, doi: [10.1093/mnras/stac3724](https://doi.org/10.1093/mnras/stac3724)
- Saha, M. N. 1920, PMag, 40, 472, doi: [10.1080/14786441008636148](https://doi.org/10.1080/14786441008636148)
- Shive, H.-Y., ZuHone, J. A., Goldbaum, N. J., et al. 2018, MNRAS, 481, 4815, doi: [10.1093/mnras/sty2586](https://doi.org/10.1093/mnras/sty2586)
- Schneider, E. E., & Robertson, B. E. 2015, ApJS, 217, 24, doi: [10.1088/0067-0049/217/2/24](https://doi.org/10.1088/0067-0049/217/2/24)
- Shapiro, P. R., & Kang, H. 1987, ApJ, 318, 32
- Sirignano, J., & Spiliopoulos, K. 2018, JCoPh, 375, 1339, doi: [10.1016/j.jcp.2018.08.029](https://doi.org/10.1016/j.jcp.2018.08.029)
- Stacy, A., Greif, T. H., & Bromm, V. 2012, MNRAS, 422, 290, doi: [10.1111/j.1365-2966.2012.20605.x](https://doi.org/10.1111/j.1365-2966.2012.20605.x)
- Stone, J. M., Mullen, P. D., Fielding, D., et al. 2024, ApJS submitted, arXiv:2409.16053, doi: [10.48550/arXiv.2409.16053](https://doi.org/10.48550/arXiv.2409.16053)
- Sugimura, K., Matsumoto, T., Hosokawa, T., Hirano, S., & Omukai, K. 2020, ApJL, 892, L14, doi: [10.3847/2041-8213/ab7d37](https://doi.org/10.3847/2041-8213/ab7d37)
- Sugimura, K., Matsumoto, T., Hosokawa, T., Hirano, S., & Omukai, K. 2023, ApJ, 959, 17, doi: [10.3847/1538-4357/ad02fc](https://doi.org/10.3847/1538-4357/ad02fc)
- Sugimura, K., Omukai, K., & Inoue, A. K. 2014, MNRAS, 445, 544, doi: [10.1093/mnras/stu1778](https://doi.org/10.1093/mnras/stu1778)
- Sulzer, I., & Buck, T. 2023, arXiv e-prints, arXiv:2312.06015, doi: [10.48550/arXiv.2312.06015](https://doi.org/10.48550/arXiv.2312.06015)
- Susa, H. 2013, ApJ, 773, 185, doi: [10.1088/0004-637X/773/2/185](https://doi.org/10.1088/0004-637X/773/2/185)
- Tanaka, K. E. I., & Omukai, K. 2014, MNRAS, 439, 1884, doi: [10.1093/mnras/stu069](https://doi.org/10.1093/mnras/stu069)
- Tibshirani, R. 1996, Journal of the Royal Statistical Society Series B: Statistical Methodology, 58, 267, doi: [10.1111/j.2517-6161.1996.tb02080.x](https://doi.org/10.1111/j.2517-6161.1996.tb02080.x)
- van de Bor, P., Brennan, J., Regan, J. A., & Mackey, J. 2025, OJAp, 8, doi: [10.33232/001c.142225](https://doi.org/10.33232/001c.142225)
- Wakelam, V., Herbst, E., Loison, J.-C., et al. 2012, The Astrophysical Journal Supplement Series, 199, 21, doi: [10.1088/0067-0049/199/1/21](https://doi.org/10.1088/0067-0049/199/1/21)
- Wibking, B. D., & Krumholz, M. R. 2022, MNRAS, 512, 1430, doi: [10.1093/mnras/stac439](https://doi.org/10.1093/mnras/stac439)
- Yoshida, N., Omukai, K., & Hernquist, L. 2008, Science, 321, 669, doi: [10.1126/science.1160259](https://doi.org/10.1126/science.1160259)